Multi-dimensional modelling of X-ray spectra for AGN accretion-disk outflows II

S. A. Sim[1], L. Miller[2], K. S. Long[3], T. J. Turner[4,5], J. N. Reeves[6]

[1]*Max-Planck-Institut für Astrophysik, Karl-Schwarzschildstr. 1, 85748 Garching, Germany*
[2]*Dept. of Physics, University of Oxford, Denys Wilkinson Buiding, Keble Road, Oxford OX1 3RH, U.K.*
[3]*Space Telescope Science Institute, 3700 San Martin Drive, Baltimore, MD 21218, U.S.A*
[4]*Dept. of Physics, University of Maryland Baltimore County, 1000 Hilltop Circle, Baltimore, MD 21250, U.S.A*
[5]*Astrophysics Science Division, NASA/GSFC, Greenbelt, MD 20771, U.S.A*
[6]*Astrophysics Group, School of Physical and Geographical Sciences, Keele University, Keele, Staffordshire ST5 8EH, U.K.*

7 February 2010

ABSTRACT
Highly-ionized fast accretion-disk winds have been suggested as an explanation for a variety of observed absorption and emission features in the X-ray spectra of Active Galactic Nuclei. Simple estimates have suggested that these flows may be massive enough to carry away a significant fraction of the accretion energy and could be involved in creating the link between supermassive black holes and their host galaxies. However, testing these hypotheses, and quantifying the outflow signatures, requires high-quality theoretical spectra for comparison with observations. Here we describe extensions of our Monte Carlo radiative transfer code that allow us to generate realistic theoretical spectra for a much wider variety of disk wind models than possible in our previous work. In particular, we have expanded the range of atomic physics simulated by the code so that L- and M-shell ions can now be included. We have also substantially improved our treatment of both ionization and radiative heating such that we are now able to compute spectra for outflows containing far more diverse plasma conditions. We present example calculations that illustrate the variety of spectral features predicted by parameterized outflow models and demonstrate their applicability to the interpretation of data by comparison with observations of the bright quasar PG1211+143. We find that the major features in the observed 2 – 10 keV spectrum of this object can be well-reproduced by our spectra, confirming that it likely hosts a massive outflow.

Key words: radiative transfer – methods: numerical – galaxies: active – X-rays: galaxies – galaxies: individual: PG1211+143

1 INTRODUCTION

The vast energy released in accretion by a supermassive black hole means that active galactic nuclei (AGN) could have a fundamental role in the formation and evolution of galaxies (see Cattaneo et al. 2009). This depends however on the nature of the physical mechanisms that couple the AGN to its host galaxy. One such possible AGN feedback mechanism is that of a massive outflow, launched somewhere close to the accreting black hole. It has already been shown that such flows might be able to account for observed correlations between properties of nuclear black holes and their host galaxies (see e.g. King 2003, 2005).

Direct evidence for AGN outflows and quantification of their properties, however, requires interpretation of observational data. Perhaps the best evidence for energetically important outflows around AGN comes from the detection of X-ray absorption lines identified with significantly blueshifted line transitions of highly ionized material (see Turner & Miller 2009 for a recent review of

X-ray observations of AGN). The most promising origin for mass-loss in the immediate vicinity of an accreting supermassive black hole is an accretion disk wind. Hydrodynamical simulations have demonstrated that such flows are plausible (e.g. Proga & Kallman 2004). However, these simulations also suggest that disk winds are likely to be very complex and thus to interpret their spectroscopic signatures quantitatively requires detailed synthetic spectra for comparison.

In previous work (Sim 2005, Sim et al. 2008, hereafter Paper I), we developed a numerical code for computing synthetic X-ray spectra for outflow models. We showed that simply-parameterized disk wind models could readily account for strong blueshifted absorption features associated with Fe XXV and Fe XXVI and we explored some of the effects of the outflow density, geometry and ionization state on these absorption line properties. Our models also confirmed that a very highly ionized outflow could affect the X-ray spectrum in more subtle ways. In particular,

the blueshifted Fe absorption lines have associated emission features that are broad and can develop extended red-skewed wings owing to the effects of electron scattering in the flow (see also Laming & Titarchuk 2004; Laurent & Titarchuk 2007). We concluded that, although complex, outflow models have the promise to simultaneously account for several of the observed X-ray spectroscopic features of AGN. We illustrated this via a direct comparison to observations of the well-known narrow line Seyfert 1 galaxy Mrk 766. However, that work was limited to the treatment of only the atomic physics necessary for the most highly ionized atomic species (specifically, He- and H-like ions). Although AGN provide copious ionizing radiation, the region responsible for the primary X-ray emission is assumed to be small and centrally concentrated. Therefore more distant portions of an outflow – or those shielded from the X-ray source by other material – need not be so significantly ionized. Thus a more realistic study requires that a wider range of ionization conditions can be considered. In particular, photoelectric absorption and/or fluorescent emission by lower ionization states of Fe may affect the X-ray spectrum, both in the Fe K region and at lower X-ray energies. For lower typical ionization conditions, the relative importance of the lighter elements also grows significantly and they can lead to strong photoelectric absorption for energies ~ 1 keV and associated discreet line features in the soft X-ray spectrum as have been reported in observations (e.g. Pounds et al. 2003, 2005; Pounds & Reeves 2007, 2009).

Here, we extend our Monte Carlo radiative transfer code described in Paper I to treat the physics of L- and M-shell ions of astrophysically abundant elements. We also substantially improve the treatment of the ionization state and introduce a simple means of estimating the kinetic temperature in the outflow, thereby eliminating this as a free parameter of the models. In addition, we modify the means by which the orientation-dependent spectra are extracted from our simulations in order to suppress the level of Monte Carlo noise. These improvements to the code and atomic data used are described in Section 2. In Section 3 we demonstrate that our improved treatment of ionization leads to quantitatively good agreement with well-known 1D codes and in Section 4 we discuss results from a calculation made with the improved code. Finally, in Section 5, we discuss the comparison of spectra computed with our models to observations of the quasar PG1211+143 before drawing conclusions in Section 6.

2   METHOD

2.1   Code overview

The code operates by performing a sequence of Monte Carlo radiative transfer simulations employing an indivisible packet scheme (see e.g. Lucy 2002, 2003). In each simulation, we follow the propagation of Monte Carlo quanta ("r-packets") representing bundles of X-ray photons through simply-parameterized models for accretion disk winds. During the r-packet propagation, the effects of Compton scattering, photoelectric absorption, bound-bound line interactions (for which the Sobolev approximation is adopted) and free-free absorption are simulated in detail. Interactions with matter (specifically bound-bound and bound-free transitions) are treated using the Macro Atom formalism introduced by Lucy (2002). This approach allows for a full treatment of line scattering, recombination and fluorescence as required to produce realistic spectra for comparison with observations. The code has also been extended to use the method of Lucy (2002, 2003) for treating both the radiative heating and cooling of matter. In this approach, when the MC

quanta undergo physical events in which the energy they represent is used to heat the plasma (e.g. by free-free absorption of photons), they are instantaneously converted to packets of thermal kinetic energy (so-called k-packets). Assuming thermal equilibrium, these k-packets are then eliminated by randomly sampling the available cooling processes (see Section 2.3). Depending on the cooling process selected, the k-packet may be converted to an r-packet which is then free to propagate. The r-packets created in this way simulate the cooling radiation emitted by the wind.

During each Monte Carlo simulation, the physical wind properties (e.g. temperature, ionization conditions etc.) are held fixed. At the end of each such simulation, the histories of the Monte Carlo quanta are used to make improved estimates of the wind properties assuming radiative, thermal and ionization equilibrium and then the Monte Carlo experiment is repeated. In this way, the wind properties are iterated to consistency with the radiation field. After the iteration cycle, a final Monte Carlo simulation is performed from which viewing-angle dependent spectra are extracted (see Section 2.7).

2.2   Ionization

To provide a more complete description of the ionization state of the outflow, the modified nebular approximation adopted in Paper I has been replaced with a detailed computation of ionization and recombination rates that are then used to solve for the steady-state ionization fractions. The following sections describe the processes that are included.

2.2.1   Photoionization

Bound-free absorption involving the ejection of an outer shell electron is included for ground states and low-energy metastable levels of all ions. During the Monte Carlo simulation, the packet trajectories are used to record estimators for the photoionization rate coefficient (γ) for each bound-free process in each of the computational grid cells of wind properties. The estimator for the rate coefficient of bound-free absorption from level j in a cell p is given by

$$\gamma_{j,k} = \frac{1}{V_p\,\Delta t}\sum_{\nu > \nu_0}\frac{a_j(\nu)}{h\nu}\epsilon\,\mathrm{d}s \qquad (1)$$

where V_p is the wind cell volume, a_j is the photoabsorption cross-section for level j (see Section 2.9) and the summation runs over all Monte Carlo quanta trajectories inside cell p when the quanta have co-moving frame frequency ν that is greater than the threshold ν_0. ϵ is the co-moving frame energy of the quantum and $\mathrm{d}s$ is the trajectory length. Δt is the time interval represented by the Monte Carlo experiment. The Doppler factor correction term for transforming the photon path length from the observer frame to the fluid frame (see e.g. Lucy 2005) is neglected for computational expediency.

At the end of a Monte Carlo simulation, the γ estimators for levels of each ion are combined to make a photoionization rate estimator for each ion (I) in each cell (p) defined by

$$\Gamma_{I,k} = \sum_{j\in I} n_{j,k}\gamma_{j,k} \Big/ \sum_{j\in I} n_{j,k} \qquad (2)$$

where the summations run over all level j of the ion for which bound-free absorption has been included in the Monte Carlo simulation. The level populations, $n_{j,k}$ are discussed in Section 2.3.4.

For L- and M-shell ions, photoabsorption involving inner shell electrons is also included. In the treatment of these processes, details of the outer electron configuration are neglected and all levels of the ion are assigned the same cross section. Following inner shell photoabsorption, the newly made ion is generally in a highly-excited state that may either decay radiatively or via ejection of one or more Auger electrons.

In the case of K-shell photoionization of L-shell ions, at most one Auger electron is expected to be produced – thus the ionization state may ultimately increase by either one or two. To incorporate this in the ionization balance, Monte Carlo estimators are used to obtain a rate coefficient for K-shell photoabsorption for each ion

$$\Gamma_{I,k}^K = \frac{1}{V_p \, \Delta t} \sum_{\nu > \nu_K} \frac{a_I^K(\nu)}{h\nu} \epsilon \, \mathrm{d}s \tag{3}$$

where the summation now runs over all packets having frequency about the K-shell edge threshold, ν_K and a^K is the K-shell photoabsorption cross-section. To obtain separate rates for single and double ionization, the mean probability ($p_I[1]$) of K-shell absorption being followed by ejection of a single Auger electron is required. This is computed using

$$p_I[1] = < \frac{\sum_i A_{ji}^a}{\sum_i A_{ji}\beta_{ji} + \sum_i A_{ji}^a} >_j \tag{4}$$

where $< ... >_j$ is a weighted mean over all states j of the ionization state $I + 1$ that are accessible by K-shell photoabsorption of ion I, $\sum_i A_{ji}^a$ is the total autoionization rate out of level j and $\sum_i A_{ji}\beta_{ji}$ is the sum of radiative decay rates incorporating the Sobolev escape probabilities β_{ji} over all downward transitions from level j. In practice, only states reached by K-shell photoabsorption from the ground configuration of ion I are included in the average and these are weighted with their statistical weights. The estimated rate at which K-shell photoabsorption in an L-shell ion increases the ionization state by one is then given by

$$\Gamma_{I,k}^K(1 - p_I[1]) \tag{5}$$

and, for double ionization,

$$\Gamma_{I,k}^K p_I[1] \quad . \tag{6}$$

Data sources for A_{ji} and A_{ji}^a are discussed in Section 2.9.

K- and L-shell photoionization of M-shell ions, are treated in a similar manner, recording a $\Gamma^{K/L}$ estimator for each such process in each grid cell. Owing to the complexity of the subsequent decays of the vacancy state (which lead to the ejection of up to three Auger electrons for K-shell ionization of the M-shell ions we consider), the Auger ejection probabilities $p_I[1]$, $p_I[2]$ and $p_I[3]$, are not computed from the atomic data set used by the code but taken from the yields tabulated by Kaastra & Mewe (1993). This approach obviates the need to follow the decay chains of the vacancy states in detail but comes at the expense of assuming that all the relevant radiative transitions are optically thin such that the M-shell ion populations are unaffected by photon trapping.

2.2.2 Collisional ionization and recombination processes

In addition to the photoionization and Auger processes described above, the ionization balance includes collisional ionization, both direct (C_{DI}) and due to collisional excitation followed by autoionization (C_{EA}), and both radiative (α^r) and di-electronic (α^d) recombination (see Section 2.9 for data sources).

2.2.3 Ionization equilibrium

At the end of each Monte Carlo simulation, the computed photoionization rate coefficients (Γ; see Section 2.2.1) are used to solve for an improved set of ion populations for each element, assuming ionization equilibrium and including all the processes described above. Since the recombination and collisional ionization terms depend on the adopted kinetic temperature (T_e), the ionization balance is iterated to consistency with the calculation of T_e (see below) for fixed Monte Carlo estimators.

2.3 Thermal balance

In Paper I, T_e was assumed to be uniform and treated as a model parameter. In order to address more general and realistic wind conditions, here we relax this assumption and obtain an estimate of T_e as a function of position via a simplified treatment of the heating and cooling rates in the wind and the assumption of thermal equilibrium.

2.3.1 Heating rates

The treatment includes heating by Compton scattering, free-free absorption and bound-free absorption of the X-ray radiation field described by the Monte Carlo simulations. Estimators for each of these heating processes in each grid cell can be readily constructed following Lucy (2003). For Compton scattering, the heating rate in a grid cell (p) is given by

$$H_p^C = \frac{n_e}{V_p \, \Delta t} \sum \bar{f}(\nu) \, \sigma(\nu) \, \epsilon \, \mathrm{d}s \tag{7}$$

where the summation runs over all packet trajectories within the grid cell p, $\sigma(\nu)$ is the Compton cross-section for the frequency (ν) of the packet and $\bar{f}(\nu)$ is the mean energy lost per Compton scattering event. The free-free heating rate is

$$H_p^{ff} = \frac{1}{V_p \, \Delta t} \sum \kappa_{ff}(\nu) \, \epsilon \, \mathrm{d}s \quad . \tag{8}$$

Again, the summation runs over all packet trajectories in the cell. The free-free absorption coefficient is given by

$$\kappa_{ff}(\nu) = 3.69 \times 10^8 \nu^{-3} T_e^{-1/2} n_e (1 - e^{-h\nu/kT_e}) \sum_I Z_I^2 N_I \ \mathrm{cm}^{-1} \tag{9}$$

where the summation runs over all ions (I) and Z_I is the ion charge.

Heating rates for photoabsorption are obtained in a similar fashion to the ionization rate estimators in 2.2.1. For bound-free absorption involving outer shells, level-by-level estimators are recorded and used to obtain a total heating rate for each ion I,

$$H_{I,k}^{bf} = \sum_{j \in I} n_{j,k} h_{j,k}^{bf} \tag{10}$$

where

$$h_{j,k}^{bf} = \frac{1}{V_p \, \Delta t} \sum_{\nu > \nu_0} a_j(\nu) \left(1 - \frac{\nu_0}{\nu}\right) \epsilon \, \mathrm{d}s \quad . \tag{11}$$

Similarly, the heating rate due to K-shell photoabsorption by ion I is given by

$$H_{I,k}^{K} = \frac{N_I}{V_p \, \Delta t} \sum_{\nu > \nu_K} a_I^{K}(\nu) \left(1 - \frac{\nu_K}{\nu}\right) \epsilon \, \mathrm{d}s \quad . \tag{12}$$

All other possible heating sources are neglected, including any contributions from outside the spectral region of the simulated radiation field or by any non-radiative processes.

2.3.2 Cooling rates

Cooling rates are required for both the treatment of k-packets (see Section 2.6) and to obtain an estimate of the local kinetic temperature. Cooling due to radiative recombination, electron collisional excitation, free-free emission, Compton cooling by low-energy photons and the adiabatic expansion of the outflow are included in this calculation.

The cooling rates due to spontaneous radiative recombination $C_{I,k}^{bf}$ and electron collisional excitation $C_{I,k}^{cl}$ are obtained following exactly Lucy (2003; his equations 31 and 33). The free-free cooling rate is

$$C_p^{ff} = 1.426 \times 10^{-27} T_e^{1/2} n_e \sum_I Z_I^2 N_I \ \mathrm{ergs \ cm^{-3} \ s^{-1}} \tag{13}$$

where we follow Lucy (2003) in setting the mean Gaunt factor to one. The adiabatic rate cooling rate is approximated by

$$C_p^{a} = 1.5 n_g k T_e \boldsymbol{\nabla} \cdot \boldsymbol{v} \tag{14}$$

where n_g is the total particle density and $\boldsymbol{\nabla} \cdot \boldsymbol{v}$ is the divergence of the velocity, evaluated at the midpoint of the cell.

The cooling rate for a population of non-relativistic electrons due to Compton up-scattering of low-energy photons ($h\nu << kT_e$) can be estimated from the local energy density of such photons U_γ via

$$C_p^{C} = 4\sigma_T U_\gamma \frac{kT_e}{m_e c} \tag{15}$$

where σ_T is the Thomson cross-section (see Frank et al. (2002), p. 180). The cooling rate due to Compton up-scattering of photons is expected to be dominated by interactions with the low energy photons originating from the accretion disk since they should significantly outnumber the X-ray photons for which our detailed radiative transfer calculations are performed. An accurate treatment of Compton cooling would therefore require that the entire bolometric light output of the system be considered. However, since our primary concern is only to obtain a reasonable estimate of the kinetic temperature, we avoid this complication and derive an estimate for the local value of U_γ from the total bolometric luminosity of the source (L_{bol}, which is treated as an input parameter for the model) and an assumption of spherical geometric dilution, i.e.

$$U_\gamma = \frac{L_{\mathrm{bol}}}{4\pi r^2 c} \tag{16}$$

where r is the distance from the centre of the grid cell to the coordinate origin. This expression is only a crude estimate for U_γ since it neglects both the geometry of the emission regions for low-energy photons (i.e. it assumes a centrally concentrated point source) and the opacity of the outflow to low-energy photons. Nevertheless, it provides a convenient estimate of the Compton cooling rate that introduces no additional computational demands and should be reasonably accurate, at least for the inner (hottest) regions of the wind.

2.3.3 The kinetic temperature determination

To obtain the kinetic temperature (T_e) for each grid cell, the radiative heating rates computed from the Monte Carlo simulation are compared with cooling rates to estimate the temperature at which thermal equilibrium,

$$H_p^{C} + H_p^{ff} + \sum_I (H_{I,k}^{bf} + H_{I,k}^{K}) = C_p^{ff} + C_p^{a} + C_p^{C} + \sum_I (C_{I,k}^{bf} + C_{I,k}^{cl}) \tag{17}$$

is established. In practice, the thermal balance equation (equation 17) is solved iteratively with the ionization balance equations to obtain self-consistent estimates of both the ionization fractions and T_e for each grid cell.

2.3.4 Excitation

In principle, the excitation state should be obtained from the statistical equilibrium equations. However, to do so would require computation and storage of estimators for all bound-bound transitions in every cell which is prohibitive for large computational grids. Therefore, we adopt a very simplified treatment of excitation, namely we use the Boltzmann distribution at the local kinetic temperature

$$\frac{n_i}{n_{\mathrm{g.s.}}} = \frac{g_i}{g_{\mathrm{g.s.}}} \exp(-\epsilon_i/kT_e) \tag{18}$$

where n_i is the population of a state with statistical weight g_i and energy ϵ_i, relative to the grounds state (g.s.). For the wind models we will describe in Sections 4 and 5, our simplified treatment of excitation is not expected to significantly affect the Fe Kα region of the spectrum since the line features which form there are mostly associated with low excitation states of high-ionization state material. The soft regions ($\lesssim 1$ keV) are more likely to be affected owing to the large numbers of transitions between excited states of L-shell Fe and Ni ions which contribute to the opacity at these photon energies.

2.4 Monte Carlo simulations

The radiation transport simulations are performed using the scheme described in Sections 3.1 to 3.3 of Paper I, modified as described below.

2.4.1 Initialization of packets

As in Paper I, an initial power-law spectrum of packet energies is adopted but the input spectrum now extends from 0.1 keV up to 511 keV to allow comparison with observational constraints from instruments with significant effective area at relatively high photon energies.

To account for the effects of a small but non-zero angular size of the X-ray emission region, the packets are no longer initialized exactly at the coordinate origin but in a spherical region around the origin. The radial extent of the emission region, r_{er}, is a parameter in the model and is generally chosen to be several gravitational radii, as appropriate for an X-ray emission region of size comparable to the innermost radii of an accretion disk.

2.4.2 Propagation of packets

Compton scattering, bound-free absorption and line absorption are treated exactly as described in Paper I, except that bound-free absorption by a few low-lying metastable levels is included for most ions.

Free-free opacity from all ions is included using equation 9. Following free-free absorption, packets are always converted to thermal energy (k-packets; see Lucy 2003).

K-shell photoionization is included as an opacity source for all L-shell and M-shell ions. Details of the outer electron configuration are neglected such that all states of an ion contribute to the same opacity term. When K-shell photoabsorption occurs in the simulations, the packet either activates a macro atom or is converted to a k-packet – this is exactly analogous to the treatment of outer-shell bound-free processes which are discussed in detail by Lucy (2003). Here, the probability of k-packet conversion is simply given by

$$p_k = 1 - \nu_K/\nu \qquad (19)$$

where ν is the absorption frequency and ν_K is the relevant K-shell absorption edge frequency. If the outcome of K-shell photoionization is activation of a macro atom, the state activated must have a K-shell vacancy in its configuration and will generally be highly excited [1]. Which of the K-shell vacancy states in the newly formed ion is activated is chosen randomly by sampling the statistical weights of the viable states in the atomic data set.

2.4.3 Macro Atom processes

The macro atom treatment used in Paper I has been extended to incorporate autoionization, bound-free transitions from excited states and K-shell photoionization.

Autoionization allows activated macro atom states to deexcite by conversion to a k-packet and to make internal transition to higher ionization states. Following the argumentation of Lucy (2002), the deactivation probability (macro atom $\rightarrow$ k-packet)

$$p^D = N_i A_a (\epsilon_i - \epsilon_f) \qquad (20)$$

where A_a is the rate coefficient ($[\mathrm{s}^{-1}]$) for autoionization from initial state i to final state f, ϵ_i and ϵ_f are the energies (excitation plus ionization) of the states, and N_i is the normalization factor. Similarly, the probability of making an internal macro atom jump $i \rightarrow f$ is

$$p^J_{i \rightarrow f} = N_i A_a \epsilon_f \quad . \qquad (21)$$

This formulation requires that the autoionization process connects two well-defined states in the atomic data set. In our calculations, this is done for L-shell ions using level-to-level autoionization rates (see Section 2.9 for data sources). However, for the M-shell ions we do not consider the target level in detail but assume that the energy flow in the autoionization process is dominated by the energy carried by the Auger electron – i.e. we assume that $\epsilon_f << \epsilon_i$ such that $p^J/p^D \approx 0$. This has the advantage that we do not require atomic level-to-level autoionization rates but only total Auger-widths for vacancy states, as are available from the literature (see Section 2.9).

For L-shell ions di-electronic recombination, is also included in the macro atom scheme. Di-electronic rate coefficients, α_d, are obtained from A_a in the usual manner and used to formulate an internal transition probability between the states

$$p^J_{i \rightarrow f} = N_f \alpha_d \epsilon_f n_e \qquad (22)$$

where n_e is the local electron number density. Note that, as for e.g. bound-free absorption, there is no macro-atom deactivation probability associated with α_d.

The γ estimators described in Section 2.2.1 are used to compute bound-free macro-atom internal transition probabilities following Lucy (2003). In all such cases, it is assumed that the relevant upper state is the ground state of the target ion. Similarly, the γ^K estimators are used to include internal transitions associated with inner shell ionization. These are applied to all energy levels of the absorbing ion lying below the first ionization potential and connect to K-vacancy states of the next higher ionization state. The choice of which K-vacancy state to activate following an internal transition is made by randomly sampling their statistical weights. L-shell ionization of M-shell ions is not included in the macro atom treatment.

2.5 Accretion disk

We assume that the black hole is surrounded by an optically thick accretion disk that lies in the xy-plane and extends from an inner radius r_d outwards throughout the simulation domain. r_d is treated as a model parameter but set equal to $6\,r_g$ (where $r_g = GM_{bh}/c^2$) for all the simulations performed here. During the Monte Carlo simulations, we also assume that all photon packets that strike the disk are lost to the X-ray regime and they are removed from the simulation.

For our particular choice of source geometry, the disk subtends a modest solid angle as seen by the X-ray source (~ 2.8 sr), meaning that a fraction of the primary X-ray photons strike the inner regions of the disk directly, without interaction in the wind.[2] The total flux striking the disk, however, is greater than this since the wind effectively causes irradiation of the outer parts of the disk via scattering and emission in the wind. Physically, these photons will interact with the disk and may lead to an additional component of disk reflection in the X-ray spectrum. We neglect any such component here but it will be investigated in a future study.

2.6 Thermal emission and k-packets

In paper I, it was assumed that energy packets converted to k-packets would be lost to the hard X-ray band. However, since cooling rates are now computed in order to impose thermal equilibrium

---

[1] Conversely, following activation by outer-shell bound-free absorption, macro atoms are always assumed to be in the ground state of the newly formed ion.

[2] This fraction, however, is not physically meaningful in our model since it is merely determined by our simple choice for the geometry of the X-ray emitting region.

(Section 2.3.2), these are now used to re-emit the packet, thus simulating the thermal emission of the outflow.

When conversion to a k-packet occurs, the cooling terms described in Section 2.3.2 are first randomly sampled to choose a cooling process. If C^a is chosen, the energy is assumed to be lost to the radiation field. The collisional cooling processes (C^{cl}) lead to activation of a macro atom state, the particular state being chosen by sampling the terms contributing to C^{cl} (see Lucy 2003). The full macro atom machinery then determines the outcome of this event.

Choosing C^{fb} or C^{ff} leads to conversion to photon packets. Both processes are assumed to emit isotropically in the co-moving frame and the emission frequency is selected using equations 26 and 41 of Lucy (2003). Note that this emission rule for bound-free processes is not exact here since it assumes a simplified cross-section shape but it is significantly less computationally demanding that sampling the real emissivity and is adequate for current purposes.

2.7   Extraction of spectra

Although spectra may be obtained by directly binning the emergent packets by frequency and direction of travel, as done in Paper I, this has the disadvantage that very large numbers of quanta must be simulated to suppress Monte Carlo noise, particularly when the spectrum is expected to depend strongly on the observer line-of-sight. As discussed by e.g. Lucy (1999), that approach is far from optimal and does not make full use of the packet trajectories during the Monte Carlo simulation. Ideally, volume-based Monte Carlo estimators should be used to obtain emissivities throughout the volume of the simulation and used to obtain spectra via a formal solution of the radiative transfer equation (see discussion e.g. Lucy 1999). However, this approach is very demanding of memory resources: for our atomic data set (with 10^5 atomic processes) and computational grids (100×100 wind cells), it ideally requires the storage of $\sim 10^9$ floating-point estimators which is prohibitive. Therefore we extract spectra using a approach similar to that implemented in the disk-wind simulations of Long & Knigge (2002) which, although less efficient, does not make significant demands on memory consumption.

Viewing-angle dependent spectra are only extracted during the final Monte Carlo simulation, once the ionization and thermal properties of the outflow have been iterated to consistency with the radiation field. The set of lines-of-sight for which spectra are required is pre-specified and then every *physical* event (meaning emission or scattering of a photon-packet) that occurs in the Monte Carlo simulations is used to compute a contribution to each of the spectra in the following manner.

When a physical event takes place in the Monte Carlo simulation, the propagation of the packet is temporarily suspended and the probability per unit solid angle of the the associated photon-packet having been scattered into each of the requested lines-of-sight is computed, $dP(\boldsymbol{n})/d\Omega$ where the vector $\boldsymbol{n}$ identifies the line-of-sight. Depending on the physical process responsible for the packet emission/scattering, $dP(\boldsymbol{n})/d\Omega$ may depend on previous properties of the packet (e.g. its incoming direction in the case of Compton scattering) or on the local outflow properties (e.g. the Sobolev escape probability in the case of line emission). We then integrate the total optical depth, $\tau(\boldsymbol{n})$, from the position of the physical event to the edge of the wind in the direction $\boldsymbol{n}$. $\tau(\boldsymbol{n})$ is computed exactly as in the Monte Carlo simulation, incorporating contributions from all physical processes included in the code and allowing for Doppler shifts to bring the photons into resonance with spectral

Table 1. Elements and ions that are included in the radiative transfer calculations.

Element	Ions	Element	Ions
C	IV – VII	S	VIII – XVII
N	V – VIII	Ar	X – XIX
O	VI – IX	Ca	XII – XXI
Ne	VIII – XI	Fe	X – XXVII
Mg	IV – XIII	Ni	XII – XXIX
Si	VI – XV		

lines. With $dP(\boldsymbol{n})/d\Omega$ and $\tau(\boldsymbol{n})$ computed, we then add an energy contribution from the event to the spectrum associated with direction $\boldsymbol{n}$ of

$$\epsilon_{rf} \frac{dP(\boldsymbol{n})}{d\Omega} e^{-\tau(\boldsymbol{n})} \qquad (23)$$

where ϵ_{rf} is the rest-frame energy of the packet and the contribution is added to the frequency bin associated with the rest-frame frequency of the packet. This calculation is repeated for each of the lines-of-sight for which spectra have been requested and then the Monte Carlo simulation proceeds until the next physical event occurs. In this way, we obtain high signal-to-noise spectra without resorting to coarse angular binning of the emergent spectra or requiring the storage of prohibitively large numbers of Monte Carlo estimators.

2.8   Rescaling of model parameters

Although our numerical simulations are performed adopting a particular value for the mass of the central black hole (M_{bh}), the spectra obtained are applicable for other M_{bh}-values following a rescaling of the dimensional wind parameters. Specifically, the ionization state, optical depths and velocity-law in the wind are preserved under a global rescaling where all the model luminosity parameters (L_{bol}, L_X) scale with the Eddington luminosity (L_{Edd}), all lengths (r_{min}, r_{max}, d, R_v, r_d and r_{em}) are scaled to the gravitational radius (r_g) and the mass-loss rate ($\dot{M}$) is scaled to the Eddington accretion rate ($\dot{M}_{Edd}$).

2.9   Atomic data

Table 1 lists the elements and ionization stages for which atomic models are included in the radiative transfer calculations. Compared to Paper I, the L-shell ions of the astrophysically abundant intermediate-mass and iron group elements have been added (Mg, Si, S, Ar, Ca, Fe and Ni). The highest M-shell ions (down to the Cl-like ion) have also been added for Fe and Ni. The solar element abundances of Asplund et al. (2005) are adopted.

In all cases, inner-shell photoionization cross-sections were taken from the fits by Verner & Yakovlev (1995). We note that, although convenient, those data do not account for smoothing of the K edges by broad resonances below threshold (see Palmeri et al. 2002; Kallman et al. 2004). Depending on the ionization state, this effect could be critical for quantitative analysis of the region around the Fe K edge but it is not important for the He- and H-like ions which dominant in most of the wind models we describe in Sections 4 and 5. For outer-shell photoionization from ground configurations (and also low-lying metastable states), cross-sections were taken from Verner et al. (1996) and a simple hydrogenic approximation was used for cross-sections from more highly excited states.

Atomic energy levels, bound-bound A-values and electron collision strengths were extracted from the CHIANTI atomic database, version 5 (Dere et al. 1997; Landi et al. 2006) for all the included L- and M-shell ions of C to Fe. For the M-shell ions of Fe, the data were limited to those of the configurations included in the study by Mendoza et al. (2004). In all cases, the T_e dependence of the electron collision strength was neglected and the low-temperature limit adopted.

Autoionization rates for K-vacancy states in L-shell ions of Fe were taken from Palmeri et al. (2003) and Auger widths for the K-vacancy states of the M-shell Fe ions from Mendoza et al. (2004). The total autoionization rates for the K-vacancy states of Mg, Si, S, Ar and Ca were taken from Palmeri et al. (2008) and the branching ratios of the autoionization process into the specific final states of the target ion were assumed to be the same for the iso-electronic Fe ion.

For the included L- and M-shell ions of Ni (XII – XIX), energy levels, Einstein A-values and total Auger widths were taken from Palmeri et al. (2008). Again, the L-shell autoionization branching ratios were assumed to be the same as in the iso-electronic Fe ion.

Radiative recombination rates are taken from Gu (2003b), where available, or else from Verner & Ferland (1996) (H-, He- and Li-like ions of C, N, O and Ne and Na-like ions of Fe and Ni), Arnaud & Raymond (1992) (Fe XVI) or Shull & van Steenberg (1982b,a), otherwise. Di-electronic rates were obtained from Gu (2003a), supplemented by those from Arnaud & Raymond (1992) (M-shell Fe ions), Shull & van Steenberg (1982b) (M-shell Ni ions) and Arnaud & Rothenflug (1985) (He- and Li-like C, N, O and Ne). Collisional ionization rate coefficients (C_{DI} and C_{EA}) are obtained from Arnaud & Raymond (1992) for Fe and Arnaud & Rothenflug (1985) for all other elements.

2.10 Wind models

The modification described above mean that the code is now capable of simulating all the necessary atomic physics to compute X-ray spectra for wind models and several such calculations will be presented in the Sections below.

For the moment, we continue to work with the simply-parameterized, smooth outflow models exactly as described in Paper I. This approach allows us to investigate outflow signatures and their sensitivity to the major wind parameters in a relatively simple manner. In the future, however, we plan to extend our studies to models that go beyond the smooth, steady-state flow prescriptions we adopt here. Numerical simulations clearly suggest that outflows are likely to have complex structure that will affect the observed spectra (see e.g. Proga & Kallman 2004; Schurch et al. 2009) and time variation in the outflow properties may well have a role in explaining the observed time dependence of some spectral features.

3 TEST OF IONIZATION BALANCE

The most significant improvements in the physics of the current code compared to that described in Paper I are the extension to lower ionization states and the substantially more sophisticated treatment of the ionization balance. To test these improvements, we have made a simple comparison with the ionization balance in the well-known photoionization radiative transfer code CLOUDY (version 07.02, last described by Ferland et al. 1998). For the test, we used a wind model with very low column density such that it would be optically thin and every cell would be illuminated with the pure
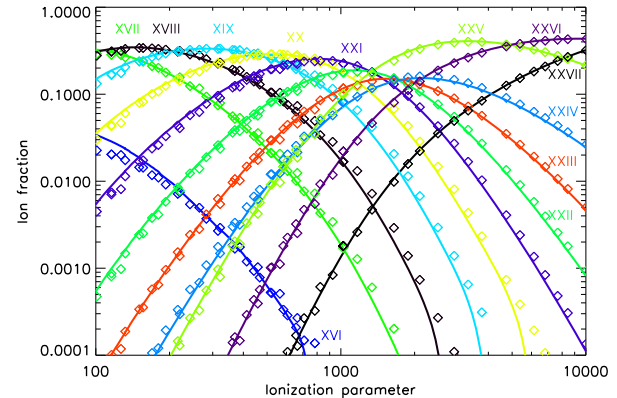

Figure 1. Ionization fractions as a function of ionization parameter for Fe XVI – XXVII computed for optically thin conditions with CLOUDY (solid lines) and our Monte Carlo code (diamond symbols). In both calculations, a power-law continuum with photon index $\Gamma = 1.2$ and a kinetic temperature of $T_e = 10^6$ K were adopted.

power-law continuum from the X-ray point source. A primary photon power-law index of $\Gamma = 1.2$ was used for the test and the kinetic temperature was forced to be 10^6 K everywhere. Ionization fractions were computed using the full machinery of our code and the results for Fe ions are plotted in Figure 1 versus an ionization parameter defined as

$$\xi = \frac{L_{0.1-50}}{r^2 n_H} \tag{24}$$

where $L_{0.1-50}$ is the source luminosity between 0.1 and 50 keV. The Fe ionization fractions obtained with CLOUDY for a low column-density spherical shell are over-plotted for comparison.

The agreement between the ionization calculations in the two codes is very good, better than 10 per cent for most of the K- and L-shell ions of iron. This precision is comparable to the accuracy of the source atomic data. Our calculations become less reliable for ionization parameters much below $\xi \sim 100$ ergs cm s^{-1} since our current atomic data set does not contain all the necessary ions (in our test calculation, Fe IX – which we neglect – has a significant role in the CLOUDY ionization balance below $\xi \sim 50$ ergs cm s^{-1}).

4 EXAMPLE CALCULATIONS

4.1 Model parameters

Here we present details of two outflow models computed with the improved code. The first, Model A has the same outflow parameters as the example model described in Paper I. However, the physical properties of the flow differ slightly from Paper I since the kinetic temperature is no longer a parameter but is determined as described in Section 2.3.3. Also, since the new code version allows for a finite spatial extent of the primary X-ray emission region and occultation of the scattered/reprocessed light (see Section 2.5), the relative amplitudes of the direct and scattered/reprocessed components of the spectrum are altered (see Section 4.3).

Our second model, Model B, has parameters chosen to illustrate the effects of lower ionization state material in the wind as can now be treated with the improved code version. We adopted a black-hole mass of 10^7 M$_\odot$ and an outflow that is wider than

those considered in Paper I, extending across a factor of three range of launching radius on the disk (50 – 150 r_g). Since the ionizing source is centrally concentrated this means that the ionization gradient across the wind (which was already present in Paper I) now extends to even lower ionization states around the outer edge. We have also chosen a more gradually accelerated outflow with lower terminal velocity. Specifically, we adopt a larger value of the velocity-law acceleration length parameter R_v (which specifies how far downstream the outflow reaches one half of the terminal speed; see equation 1 of Paper I) and a smaller value of f_v (which relates the terminal speed to the escape speed at the base of a streamline; see equation 2 of Paper I). The X-ray source parameters and the wind mass-loss rate for Model B were motivated by previous studies of the bright quasar PG1211+143 with which more detailed comparisons are made in Section 5. The primary X-ray source luminosity and the total bolometric luminosity were chosen to give ratios to the Eddington luminosity (L_{Edd}) similar to those inferred for PG1211+143: adopting a typical 2 – 10 keV luminosity of 10^{44} ergs s^{-1} and bolometric luminosity of 4×10^{45} ergs s^{-1} (Pounds et al. 2003) yields $L_X/L_{Edd} \sim 0.02$ and $L_{bol}/L_{Edd} \sim 0.8$ for a black hole mass $\sim 4 \times 10^7$ M$_\odot$ (Kaspi et al. 2000) and accretion efficiency of ~ 0.06. The power-law index ($\Gamma \sim 1.8$) and mass-loss rate ($\dot{M} \sim \dot{M}_{Edd}$) were also chosen to be roughly appropriate for PG1211+143, as motivated by the discussion of Pounds et al. (2003).

The complete set of model parameters is given in Table 2; definitions of the geometry and velocity-law parameters are given in Paper I. For both models, we placed the innermost edge for the accretion disk at the last stable orbit for a Schwarzschild black hole ($6r_g$) and assumed a comparable size for the region of X-ray emission (again $6r_g$).

4.2 Thermal and ionization structure

Figure 2 shows the distribution of kinetic temperature and Fe ionization states in the example models. For Model A, the spatial variation of the ionization state is qualitatively similar to that discussed in Paper I: the inner edge of the wind is almost fully ionized and gradients of decreasing ionization occur both along the outflow and across the base of the flow. Model B is similar but, owing to the larger radial extent of the flow launching region in this model, the gradient across the flow is particularly well-developed such that a substantial region on the outside of the wind is dominated by L-shell Fe ions. As expected, the regions of the wind that are most strongly ionized are also most strongly heated by the X-ray source leading to significant kinetic temperature variations across the flow (right panels of Figure 2).

4.3 Computed spectra

For both the example models, we computed emergent spectra for twenty lines-of-sight uniformly sampling the orientation ($0 < \mu < 1$, where $\theta = \cos^{-1} \mu$ is the angle between the line-of-sight and the rotation axis). Figures 3 and 4 show the computed spectra for five of these lines-of-sight for Models A and B, respectively. The orientations of the chosen lines-of-sight are indicated by the dashed lines in Figure 2. As in Paper I, the propagation histories of the Monte Carlo quanta are used to divide the emergent spectrum into a direct component (representing photons that reached the observer without any interactions) and a scattered/reprocessed component derived from the quanta that underwent at least one interaction in

the wind. These contribution are separately plotted in the left panels of Figures 3 and 4. The right panels show the 2 – 10 keV region of the spectra in greater detail.

The first line of sight shown for both models (top panels of Figures 3 and 4) corresponds to an observer at sufficiently low inclination that no portion of the wind obscures the primary X-ray source. Thus the direct component of radiation is unaffected by the wind (red line in top left panels). However, since the outflow scatters light from other lines-of-sight and produces its own thermal emission, the direct light is supplemented by a significant component of scattered/reprocessed radiation. As one would expect, this scattered/reprocessed spectrum is qualitatively similar to that obtained from standard disk reflection models (e.g. Ross & Fabian 2005). In particular, a moderately strong Fe Kα emission line appears in both models. This is predominantly formed by Fe XXV and XXVI since most of the wind reflection seen from this line-of-sight occurs in the highly-ionized inner surface of the outflow. The emission line profile is Doppler broadened and, owing to the substantial outflow velocities, develops an electron scattering wing (Auer & van Blerkom 1972; Laurent & Titarchuk 2007) that skews the profile to the red (for both models, it extends down to ~ 5 keV for this line-of-sight). At softer energies, the spectrum of scattered Monte Carlo quanta also contains a variety of other emission features. These are considerably stronger in Model B owing to the greater range of ionization conditions in the wind. In this model, weak but distinct Kα emission lines of O, Si and S (~ 0.65, 2.0 and 2.6 keV, respectively) are present together with forests of blended lines from the L-shell ions of Fe. The emission profiles of these features are broadened by the same mechanisms which affect the Fe K line leading to rather complex spectra. The scattered/reprocessed spectrum also adds a distinct "Compton hump" to the total spectrum, causing it to have a broad peak around 20 – 30 keV; at even harder energies the scattered/reprocessed spectrum bends down (owing to the energy dependence of the Compton cross-section) such that the flat, primary X-ray spectrum becomes increasingly dominant above about 50 keV. For this inclination angle, the spectrum computed for Model A is very similar to that obtained for the same outflow parameters using the code version in Paper I (see upper right panel of Figure 3). The main difference is a modest offset in normalization that arises from the reduced amplitude of the scattered component of radiation owing to occultation by the accretion disk which is included in the new calculations (see Section 2.5).
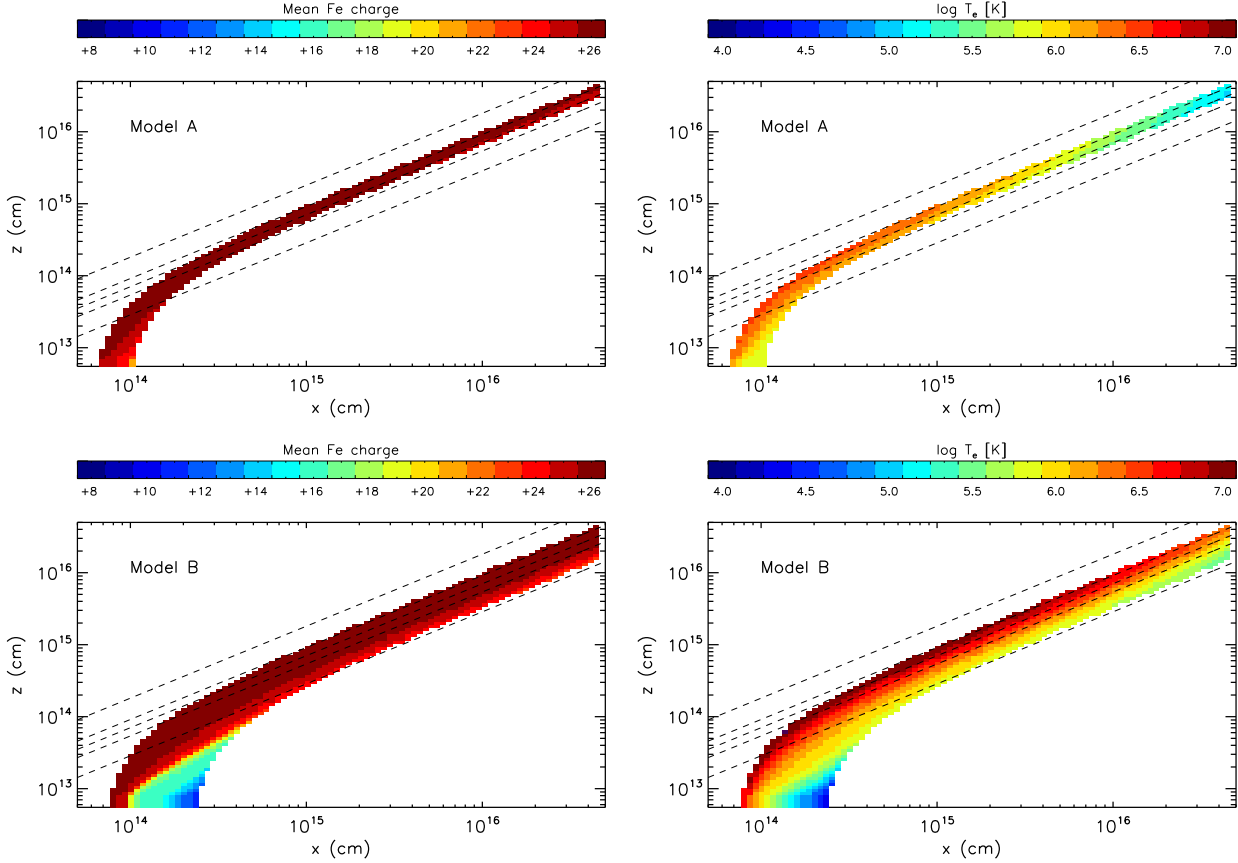
The second line of sight considered ($\mu = 0.675$) passes through the upper-most layers of the outflow models which are hottest and most highly-ionized. The remaining three lines-of-sight ($\mu = 0.575$, 0.475 and 0.275) pass through increasingly denser and cooler parts of the wind such that the spectra become more complex. As in Paper I, lines of sight through the wind show weak, narrow, blueshifted absorption features associated with highly ionized material, most importantly the Kα lines of Fe XXV and XXVI. In Model A, the spectra for $\mu = 0.675$ (and lower) are characteristically similar to that of the example model in Paper I (see comparison in Figure 3) but there are some differences in detail. In particular, with the improved code version the amplitude of the component of scattered/reprocessed light is reduced by disk occultation, the mean ionization state is slightly lower and the absorption features are sharper. This last effect arises because of the angular binning of MC quanta used to extract the spectra in Paper I: since the line-shifts depend on inclination, spectra obtained via angular binning will tend to have slightly smeared line profiles.

In Model B, the $\mu = 0.675$ line of sight has an integrated hydrogen column density of $N_H \sim 2 \times 10^{23}$ cm^{-2}, only a factor of

Table 2. Inputs parameters for the example model.

Parameter	Model A	Model B
mass of central object, M_{bh}	4.3×10^6 M$_\odot$	10^7 M$_\odot$
bolometric source luminosity, $L_{\rm bol}$	2.5×10^{44} ergs s^{-1} ($\sim 0.6 L_{\rm Edd}$)	10^{45} ergs s^{-1} ($\sim 0.8 L_{\rm Edd}$)
source luminosity (2 – 10 keV), L_X	10^{43} ergs s^{-1} ($\sim 0.02 L_{\rm Edd}$)	2.5×10^{43} ergs s^{-1} ($\sim 0.02 L_{\rm Edd}$)
source power-law photon index, Γ	2.38	1.8
range of source photon energies in simulation	$0.1 - 511$ keV	$0.1 - 511$ keV
size of emission region, r_{er}	$6 r_g = 3.8 \times 10^{12}$ cm	$6 r_g = 8.9 \times 10^{12}$ cm
inner radius of disk, r_d	$6 r_g = 3.8 \times 10^{12}$ cm	$6 r_g = 8.9 \times 10^{12}$ cm
inner launch radius, $r_{\rm min}$	$100\,{\rm r}_g = 6.4 \times 10^{13}$ cm	$50\,{\rm r}_g = 7.4 \times 10^{13}$ cm
outer launch radius, $r_{\rm max}$	$1.5 r_{\rm min}$	$3 r_{\rm min}$
distance to wind focus, d	$r_{\rm min}$	$r_{\rm min}$
terminal velocity parameter, f_v	1.0	0.5
velocity scale length, R_v	$r_{\rm min}$	$3 r_{\rm min}$
velocity exponent, β	1.0	1.0
launch velocity, v_0	0.0	0.0
wind mass-loss rate, $\dot{M}$	0.1 M$_\odot$ yr^{-1} ($\sim 0.6 \dot{M}_{\rm Edd}$)^a	0.38 M$_\odot$ yr^{-1} ($\sim \dot{M}_{\rm Edd}$)^a
mass-loss exponent, k	-1.0	-1.0
outer radius of simulation grid	5×10^{16} cm	5×10^{16} cm
3D Cartesian RT grid cells	$180 \times 180 \times 180$	$180 \times 180 \times 180$
2D wind grid zones	100×100	100×100

^{a} The Eddington accretion rate, $\dot{M}_{\rm Edd}$ was computed assuming a radiative efficiency of six percent.

Figure 2. Distribution of mean Fe ionization state (left) and kinetic temperature (right) for Models A (top) and B (bottom). The dashed lines indicate the five lines-of-sight for which spectra are shown in Figures 3 and 4.
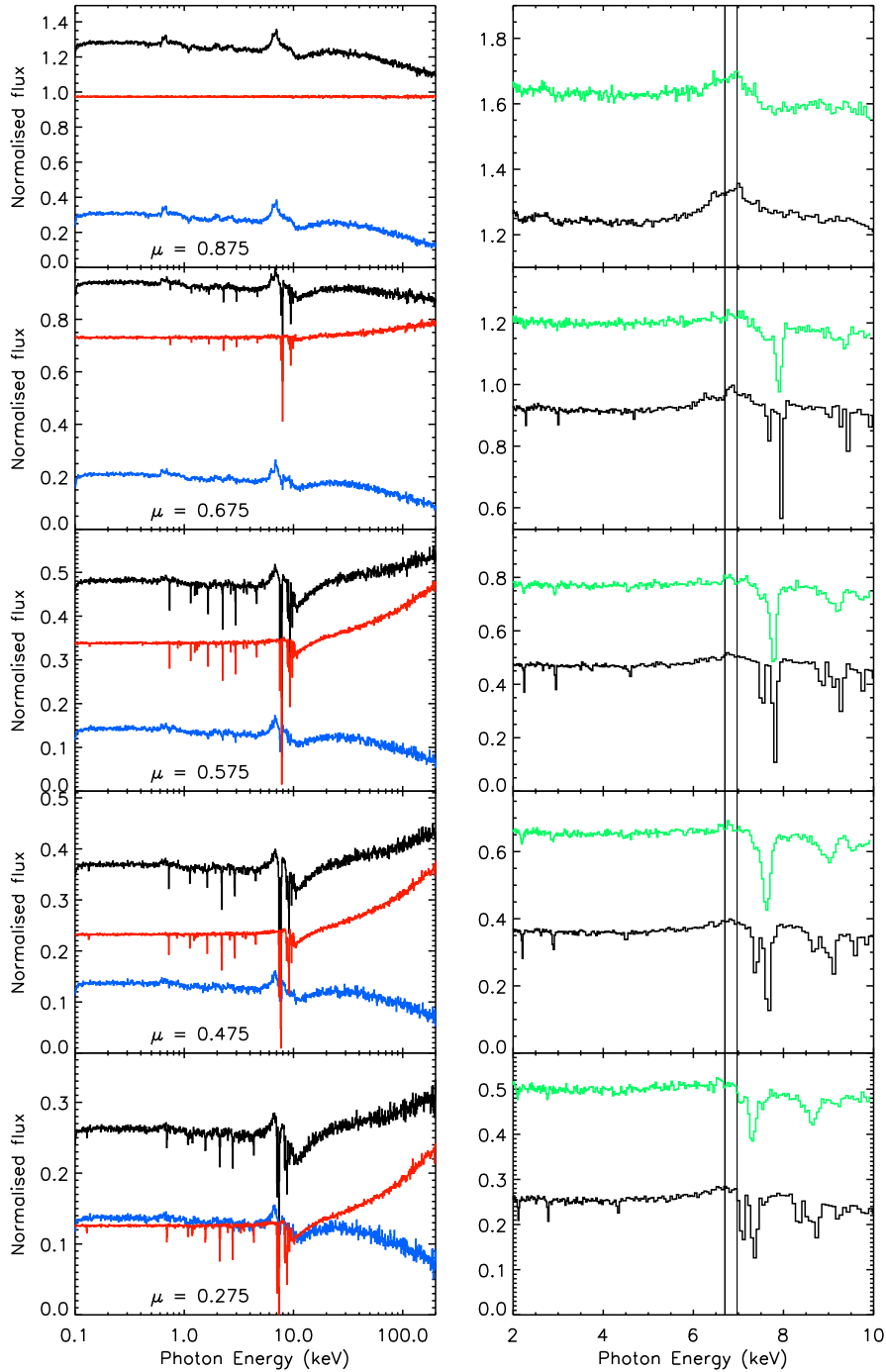
Figure 3. Spectra for five observer lines-of-sight computed from Model A (from top to bottom, $\mu = 0.875$, 0.675, 0.575, 0.475 and 0.275 where $\theta = \cos^{-1} \mu$ is the angle of the line-of-sight relative to the polar axis). The left panels show the spectrum from $0.1 - 200$ keV while the right panels show the $2 - 10$ keV region in detail for the same lines-of-sight. Note that the abscissa is plotted logarithmically in the left panels but linearly in the right panels. In the left panels, the total spectrum is shown in black, the spectrum of direct photons in red and the scattered/reprocessed spectrum in blue. In the right panels, the total spectrum computed with the new code version is plotted in black while the spectra from the example model in Paper I are shown in green, for comparison. The vertical lines indicate the mean rest energies of the Fe XXV/XXVI Kα transitions ($\sim 6.7/6.97$ keV). All the spectra are normalised to the incident X-ray spectrum which has a photon power-law index, $\Gamma = 2.38$. Monte Carlo noise from the simulations is present in all the spectra and is responsible for the small-scale fluctuations.
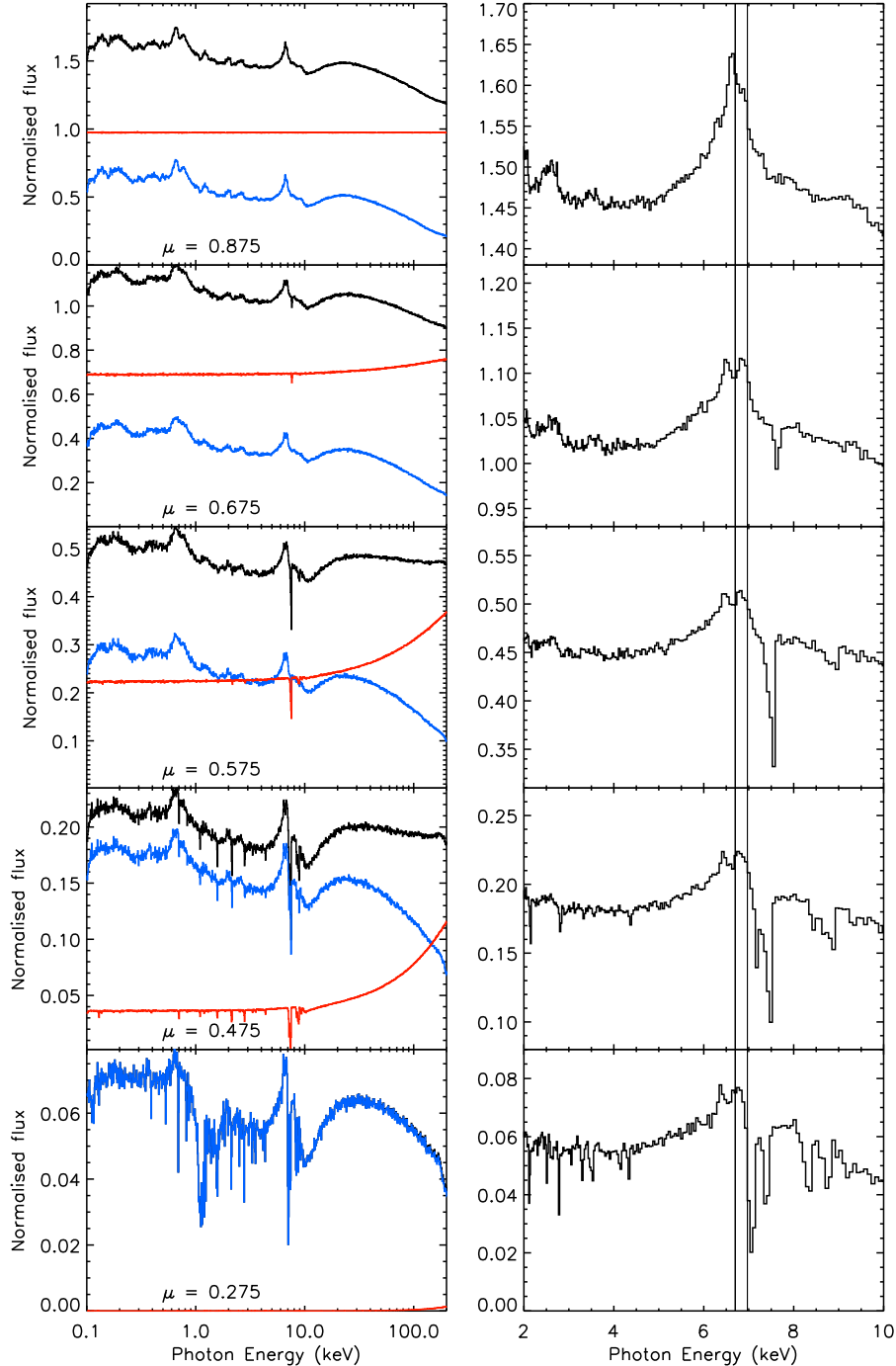
Figure 4. As Figure 3 but showing spectra from Model B. No comparison spectra are shown in the right panels. All the spectra are normalised to the incident X-ray spectrum which has a photon power-law index, $\Gamma=1.8$.

a few smaller than that suggested for the most highly ionized material in the spectrum of PG1211+143 ($\sim 5 \times 10^{23}$ cm^{-2}, Pounds et al. 2003). However, the material along this line of sight is hot and almost fully ionized (see Figure 2) such that Compton scattering is the only important opacity source. This reduces the flux of the direct component of the radiation and causes it to curve upwards at high energies, a consequence of the photon-energy dependence of the Compton cross section. Although the scattered/reprocessed component of the light still shows a significant Compton hump,

this upwards curvature of the direct component partially cancels it out leaving only a modest bump in the total spectrum. The only significant absorption feature imprinted by the wind for this line of sight is from the trace population of Fe XXVI and only the Kα line is strong enough to be plausibly detectable with current instruments. The emission features in the scattered/reprocessed spectrum are qualitatively very similar to those for the lower inclination angle described above except that the features are slightly broader thanks to the greater line-of-sight components of both the outflow and ro-

tational velocity fields for this orientation. In addition, the Fe Kα line shows two distinct peaks, one close to the rest Kα energy of Fe XXVI and the other to that of Fe XXV and the high L-shell ions.

The third to fifth lines-of-sight for which spectra are shown for Model B (Figure 4) have sufficiently high column densities ($N_H \sim 10^{24}$, $\sim 4 \times 10^{24}$ and $\sim 10^{25}$ cm^{-2}, respectively) that the direct component of radiation is almost completely blocked except at rather high energies ($\gtrsim 30$ keV). For the highest inclination angle considered ($\mu = 0.275$), the reprocessed component of light dominates even well above 100 keV such that the total spectrum of the wind shows a downturn at these energies, a property that can be constrained by high-energy observations (see discussion by Fabian et al. 1995). However, we stress that for the lower inclination angles in this model, and indeed all the angles considered for Model A, the direct component rises sufficiently rapidly with energy that there is still significant flux emerging above 200 keV.

For the $\mu = 0.575$, 0.475 and 0.275 lines-of-sight, the Model B spectrum is progressively more strongly affected by absorption in the wind. The Fe Kα absorption line becomes deeper and gradually switches from being dominated by Fe XXVI to Fe XXV at higher inclination angles. The associated Kα emission line remains strong and its apparent red wing becomes increasingly extended for high inclination angles. As expected, the Fe Kα absorption is also accompanied by blueshifted absorption by Fe Kβ (~ 9.0 keV) and Ni Kα (Ni XXVII at ~ 8.5 keV and XXVIII at ~ 8.8 keV). There is also significant absorption around the blueshifted Fe K edge which, although somewhat smeared out by the Doppler shifts, causes the distinct drop in flux at around 10 keV.

At softer energies, blueshifted absorption features associated with the abundant light elements become increasingly prominent as the inclination angle is increased. For an inclination of $\mu = 0.475$ (fourth row in Figure 2), weak narrow Kα absorption lines of S XVI (~ 2.8 keV), Si XIV (~ 2.2 keV), Mg XII (~ 1.6 keV), Ne X (~ 1.1 keV) and O VIII (~ 0.71 keV) are all present but their equivalent widths are small, generally less than a few eV. Weak Fe XXIV lines also appear at ~ 1.2 and 1.3 keV due to blueshifted transitions between its ground 2p^5 configuration and states of the excited 2p^4 (^{3}P)3s configuration. At the higher inclination angle of $\mu = 0.275$ (fifth row in Figure 4), the absorption spectrum is even more complex. The Kα transitions mentioned above are all still present and generally somewhat stronger. Very weak Kα lines due to Ar and Ca also manifest (~ 3.6 and 4.4 keV, respectively), as do the Kβ lines of the H-like ions of Mg, Si and S. Although O VIII Kβ absorption is also significant in the simulation, this feature is blended with comparably strong lines of Fe XVIII and XIX. Deep absorption occurs between 1.0 and 1.3 keV owing to the forest of lines arising in transitions from the low-lying $n = 2$ configurations of Fe and Ni L-shell ions. Furthermore, there is also significant bound-free absorption by the ground states of the K-shell ions of O, Mg, Si and S and of the L-shell ions of Fe that causes a drop in the flux above ~ 1.5 keV.

5 PRELIMINARY COMPARISON WITH PG1211+143

Thanks to the extension of the capabilities of the code to deal with lower ionization conditions, we can now use the models to compare much more realistic theoretical spectra with observations to establishing how readily outflow models can explain observed spectroscopic features and, if real, what the physical properties of these flows might be. For a fully detailed comparison a large grid of theoretical models covering the physically interesting parameter space

must be computed. This will be an important next step in our studies but we begin here by making a preliminary comparison with the observed spectrum of the bright quasar PG1211+143.

5.1 Observational data

Amongst the first direct evidence for highly ionized massive outflows from AGN was a report by Pounds et al. (2003, 2005) based on the analysis of *XMM-Newton* X-ray spectra of PG1211+143. They reported the detection of several strong absorption features which they associated with blueshifted Kα transitions of C, N, O, Ne, Mg, S and Fe. To quantify the absorption features in the (1 – 10 keV) European Photon Imaging Camera (EPIC) pn spectrum they fit an XSTAR (Kallman & Bautista 2001) absorption model and found that a high column density ($N_H \sim 5 \times 10^{23}$ cm^{-2}) and a high ionization parameter ($\log(\xi/\text{ergs cm s}^{-1}) \sim 3.4$) were required to explain both the claimed Fe and S Kα absorption lines as originating in a rapid ($v \sim 0.08c$) outflow. Based on the proposed identification of the lower ionization Mg line in the EPIC pn spectrum and lines attributed to the lighter elements in their contemporaneous Reflection Grating Spectrometer (RGS) spectra, they also postulated that additional absorbing components must be present in the outflow with significantly lower column density and ionization parameter (although comparable outflow speeds). Broad emission was also identified in the EPIC pn spectrum, extending from ~ 3 to 7 keV. Although this emission feature can be fit as an extreme relativistic Fe Kα emission line originating from reflection by the inner most regions of an ionized accretion disk (Pounds et al. 2003), it has more recently been suggested that it may be P Cygni emission physically associated with the blue-shifted Kα absorption (e.g. Pounds & Reeves 2009) as would be expected from a wind with a large covering fraction.

Subsequent re-observations of PG1211+143 with *XMM-Newton* were made in 2004 (Pounds & Reeves 2007) and 2007 (Pounds & Reeves 2009). These showed that, although the spectral properties of PG1211+143 are significantly time-variable, the fast outflow of highly ionized gas is persistent and confirmed that it is likely to be an energetically important component of the system.

Given the complexity of the available data for PG1211+143 and the wide range of spectroscopic features identified in the 2001 *XMM* data first reported by Pounds et al. (2003), this object provides an excellent point of comparison with our synthetic spectra for outflows. In particular, while previous efforts to quantify the spectra have generally adopted distinct fit components for the claimed absorption lines and the apparently broad emission redward of ~ 7 keV, our wind models allow us to explore the relationship between these features with a set of physical models.

The X-ray spectrum of PG1211+143 shows a strong excess for energies $\lesssim 1$ keV relative to an extrapolation of a power-law fit to the harder energy spectrum (see e.g. Pounds et al. 2003). The origin of soft excesses in AGN spectra remains unclear: although it has been suggested that they may be a consequence of absorption by relatively low ionization material and data showing strong soft excesses (including those of PG1211+143; see Pounds & Reeves 2007, 2009) have been successfully fit assuming an absorption-dominated origin, the geometry and origin of the absorbing material is not well-constrained. In view of this uncertainty, we restrict our fitting to the 2 – 10 keV spectrum of PG1211+143 to avoid biasing our fit by a choice of particular model for the origin of the soft excess. However, we will qualitatively discuss the lower-energy absorption features predicted by the model compared to those reported in the PG1211+143 spectra.

In the following, we will make quantitative comparisons with the data set compiled by Pounds & Reeves (2009) by stacking *XMM* EPIC pn data from 2001, 2004 and 2007. We have rebinned the data to the energy-dependent half-width at half-maximum (HWHM) of the EPIC pn instrument.

5.2 Choice of model parameters

We began by making a comparison of the stacked $2-10$ keV data of PG1211+143 with our example spectra (described in Section 4). As discussed above, Model B already indicated that many of the discreet features identified in the spectrum of PG1211+143 can qualitatively be reproduced in our theoretical spectra. To produce a strong, significantly blueshifted Fe XXV/XXVI absorption feature, the example models suggest that a line-of-sight passing through some portion of the inner, highly ionized edge of the flow is required ($\mu \sim 0.4-0.6$ for the example model geometric parameters). Although Model B already produces strong Kα absorption, the blueshift is slightly too small compared to that suggested for PG1211+143 (Pounds et al. 2003, 2005; Pounds & Page 2006). Therefore, we first increased the outflow velocity parameter (f_v) from 1/2 to 2/3, a value intermediate between those used for the two example models.

Upon quantitative comparison, the Model B spectra also differ in detail from the observations of PG1211+143 in that the lower ionization features are somewhat too weak for the appropriate inclination angles (e.g. the equivalent width of the S XVI Lyα line is only $\lesssim 5$eV in the model while Pounds et al. (2005) and Pounds & Page (2006) report equivalent widths of ~ 40 and ~ 24eV, respectively). Thus, models with lower typical ionization state are desirable. In principle, a full grid of models exploring all the outflow parameters should be explored to find the best match to the observed spectrum. Here, however, we restrict ourselves to varying parameters that are expected to directly affect the mean ionization state. We therefore created a small grid of six models that explores the effects of higher wind mass-loss rates ($\dot{M}$) and longer velocity-law scale lengths (R_v) while keeping all other parameters the same as for Model B. Relatively modest numbers of Monte Carlo quanta were used for these simulations in order to reduce the computation demands (only $\sim 10^6$ packets were used for the calculation of the spectra).

The quantitative effect of $\dot{M}$ on the models was discussed in Paper I and that discussion remains applicable here. In particular, increasing $\dot{M}$ leads to higher densities and therefore lower ionization states for a fixed X-ray source luminosity. In general, it also leads to stronger absorption features thanks to the increased column density for a fixed line of sight. Our grid of models explored $\dot{M}$-values of 0.38, 0.76 and 1.52 M$_\odot$ yr^{-1} corresponding to $\sim 1, 2$ and 4 $\dot{M}_{\rm Edd}$ for our adopted value of $M_{\rm bh} \sim 10^7 M_\odot$.

The second parameter varied, R_v, affects the spectrum for two distinct reasons. First, a larger value of R_v means that the flow accelerates more gradually such that the material in the accelerating region is more dense for fixed values of $\dot{M}$ and f_v. Secondly, the larger value of R_v reduces the outflow velocity-gradient such that the Sobolev optical depths of the line transitions become larger in the acceleration region. For our grid we considered R_v-values of 3 and 5 $r_{\rm min}$.

As when making our comparison with the average spectrum of Mrk 766 in Paper I, we constructed a multiplicative table ("mtable") model for use with XSPEC (version 11, Arnaud 1996) from the ratio of our computed spectra to the primary power-law adopted in the radiative transfer simulations. We then attempted to fit the PG1211+143 data using a model comprising of a power-law (with free normalization [N] and power-law index [Γ]) combined with this mtable (which contains a total of 120 spectra from the grid of $3 \times 2 \times 20$ in $\dot{M}$, R_v and μ). Given the strong but complex dependence of the spectral features to the line-of-sight (μ) we did not allow this parameter to be fit directly but stepped through the μ-values of the grid manually, freezing this parameter and then fitting the remaining four quantities (N, Γ, $\dot{M}$ and R_v). We did not allow for any component of systematic error in any of our fits as this is not expected to have a significant effect in the fit to the $2-10$ keV region (see the discussion in Miller et al. 2009). Although other physical processes are expected to have a role in shaping the X-ray spectra of AGN (in particular, some degree of disk reflection and some warm absorber component seem all but inevitable), we did not include any additional component in this fit since our objective is to establish whether our disk wind models alone could be the dominant component that accounts for the major spectra features in the $2-10$ keV band.

For this model, the best fit was obtained for $\mu = 0.525$ (frozen), $\Gamma = 1.9$, $\dot{M} = 0.68$ M$_\odot$ yr^{-1} and $R_v = 3.2$ $r_{\rm min}$ and yielded χ^2/d.o.f of 163/132. Although an imperfect fit, this suggests that the majority of the spectroscopic features are well accounted for by the model (a pure power-law fit to the same data yields χ^2/d.o.f of 389/134).

To make a detailed comparison, we computed spectra for eighteen more models adopting parameters close to those favoured from the XSPEC fits and extending the range in R_v ($\Gamma = [1.7, 1.9]$, $R_v = [3, 5, 8]r_{\rm min}$, $\dot{M} = [0.53, 0.65, 0.76]$ M$_\odot$ yr^{-1}). For these simulations a larger number of MC quanta ($\sim 7 \times 10^6$) were used to compute the spectra. The spectra obtained from each of these simulations are qualitatively similar although the amplitude of the spectra features varies slightly. We fit spectra from these eighteen models to the $2-10$ keV spectrum in a similar manner to that described above – the best fitting spectrum obtained from this model grid (χ^2/d.o.f of 160/132) was for parameters close to that of the model with $\Gamma = 1.9$, $R_v = 8r_{\rm min}$ and $\dot{M} = 0.53$ M$_\odot$ yr^{-1} (for $\mu = 0.575$); therefore we use the spectra from this model as the basis for our comparison (see below).

5.3 Discussion

Figure 5 compares the Fe Kα spectral region for the model with $R_v = 8r_{\rm min}$, $\dot{M} = 0.53$ M$_\odot$ yr^{-1} and $\mu = 0.575$ with the unfolded data of PG1211+143 (Pounds & Reeves 2009). The comparison is shown for the photon energy scale observed at the Earth, accounting for the source redshift of $z = 0.0809$ (Marziani et al. 1996).

The agreement between model and data is generally very good and shows that the disk wind paradigm readily produces the important features that characterize these data – blueshifted Fe Kα absorption and broad red shifted Kα emission with a red-skewed wing – with strengths comparable to those observed. In agreement with the data, the model also predicts weak S XVI absorption around 2.7 keV. There are, however, some clear discrepancies. For example, additional narrow components of emission may be required in the emission line profile (see discussion by Pounds & Reeves 2009) and the model seems to predict too little absorption at around 8 keV. However, none of these details suggest that the outflow paradigm is inappropriate for these data and may simply indicate physically distinct contributions to the spectrum. E.g. any very narrow emission components required by the data are unlikely to be associated
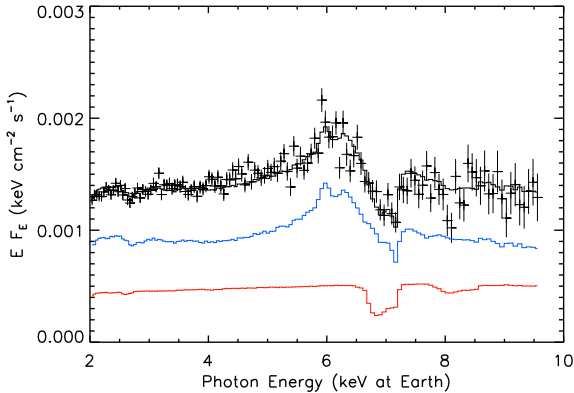
Figure 5. Comparison of the Pounds et al. (2009) stacked data for PG1211+143 (black crosses) and the wind model (black histogram) described in the text. The wind parameters are all identical to Model B (Table 2) except for $\Gamma = 1.9$, $R_v = 8r_{min}$ and $\dot{M} = 0.53$ M$_\odot$ yr^{-1}. The model spectrum shown is for a viewing inclination of $\mu = 0.575$. The red and blue histograms show the contributions to the model spectrum from direct and scattered/reprocessed radiation, respectively. The photon energy scale of the model spectrum has been adjusted to account for the redshift of PG1211+143 ($z = 0.0809$).

Figure 6. The RGS region of the spectra of the same wind model shown in Figure 5. The black histogram shows the model spectrum for $\mu = 0.575$ (same inclination as used for the fit to the stacked EPIC pn data shown in Figure 5). The green and orange histograms show the spectra for $\mu = 0.475$ and 0.375, respectively. Each spectrum is shown as a ratio to the input pure power-law spectrum which had $\Gamma = 1.9$ and renormalised to 1.0 around 30Å. The identifications with red tick marks indicate the observed energies of lines identified in the observations of PG1211+143 by Pounds et al. (2003) that are distinct in the model spectra. The black tick marks indicate lines identified in the observations that do not have significant strength in any of the model spectra. Fe XXIV (blue tick mark) is responsible for the feature are 11 Å in the $\mu = 0.475$ spectrum which was not discussed by Pounds et al. (2003).

with the high velocity wind but can be more readily attributed to reflection by low-velocity material.

Since the source is clearly complex, fitting the 2 – 10 keV spectrum to a wind model alone yields parameters that should only by regarded as indicative of those appropriate for PG1211+143. To make a quantitative comparison of our models with the lower energy spectra for PG1211+143 would requires significantly more complex fits of the data to be performed to address the strong soft excess and account for any physically distinct, lower-ionization contribution to absorption. However, at minimum, the highly-ionized wind should be able to imprint discreet blueshifted absorption and broad emission features in the softer spectrum consistent with those that have been claimed from previous analyses of the PG1211+143 RGS spectrum (e.g. Pounds et al. 2003; Pounds & Reeves 2007). [3]

To investigate this, we show in Figure 6 the 10 – 35Å spectra (c.f. figures 6 – 9 of Pounds et al. 2003) for the same wind model used in Figure 5. The spectrum is shown for the line-of-sight ($\mu = 0.575$) that best fit the Fe K region of the stacked data of Pounds & Reeves (2009) and also for two higher inclination angles ($\mu = 0.475$ and 0.375). The wavelength of blueshifted absorption lines for which identifications were claimed by Pounds et al. (2003) are indicated in the figure. Several of these – in particular those corresponding to relatively high ionization states (e.g. Ne X, O VIII, N VII, C VI) – are clearly present in the model with strength and blueshift depending sensitively on the observer's inclination. Fe XXIV imprints a clear additional absorption feature for $\mu = 0.475$ – although they did not discuss this in detail, we note that the fit in figure 9 of Pounds et al. (2003) does include an

absorption line around 11 Å. The model also predicts significantly broadened O VIII Lyman α emission, qualitatively similar to that discussed by Pounds & Reeves (2007, 2009) in their more recent analyses of the PG1211+143 RGS data. Thus our outflow models are able to simultaneously account for observable features in both the Fe K band and the softer-energy parts of the spectrum and there are good prospects that more detailed fitting of the complete set of spectral data will allow more robust constraints to be placed on the outflow model parameters.

The less ionized species (Ne IX and O VII) are present in only very small quantities in the model and do not imprint lines in the spectra shown. The presence of these lines in the data suggests that a wider range of ionization states than in the model used here is required to explain the complete 2001 RGS spectrum. This may be found by exploring a greater range of our model parameter-space but may also require us to go beyond our assumption of a smooth, steady-state flow. A more realistic model incorporating flow inhomogeneities will inevitably have a wider range of densities, and therefore ionization state. Such effects will be investigated in future studies.

The spectral model used here is too simplistic to address the strong soft excess observed in PG1211+143. However, we note that the wind model does clearly lead to an excess of emission below $\sim$ 1 keV suggesting that reprocessing by the fast flow may account for a modest fraction of the excess soft-energy emission (c.f. King & Pounds 2003). Much of this contribution is due to heavily blended forests of emission lines (including those of L-shell Fe) but there are also moderately strong discreet features, such as the broad O VIII Lyα emission line mentioned above.

We defer more detailed studies including both a wider exploration of the model parameter space and the interplay of wind-formed spectral features with other components of the system to later work but the simple comparisons presented here already sup-

---

[3] We note, however, that the exact combination of wind model and observer line-of-sight which fit the stacked EPIC pn data of Pounds & Reeves (2009) (which combines observations from 2001, 2004 and 2007) is not expected to be perfectly applicable for comparison with the RGS absorption features discussed by Pounds et al. (2003) since it is known that the spectroscopic signatures of outflow are time-variable.
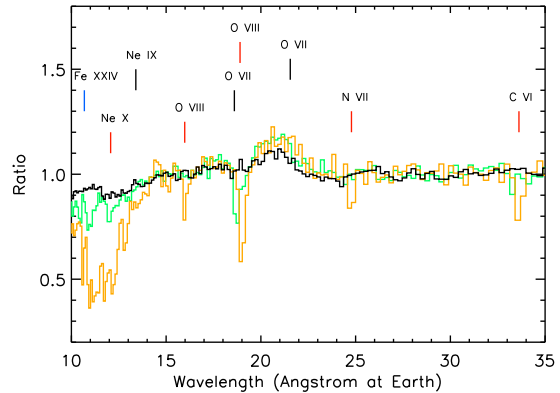
port the notion that the Fe K absorption *and* emission features could be predominantly formed in a fast outflow as in the picture presented by Pounds & Reeves (2009). Scaled to the black hole mass of PG1211+143 (4×10^7 M$_\odot$, Kaspi et al. 2000; see Section 2.8), the model with which we have compared has a mass-loss rate of $\dot{M} = 2.1$ M$_\odot$ yr^{-1} and a total covering fraction[4] of $b = 0.7$. These are comparable to the properties inferred by Pounds & Reeves (2009) and support their conclusion that the flow is very likely to be energetically important.

6 CONCLUSIONS AND FUTURE WORK

Outflows from the accretion disks around supermassive black holes are a promising explanation for the blueshifted absorption line features that have been identified in the X-ray spectra of AGN. They are also theoretically expected in high Eddington ratio sources for which line-driven winds have been modelled by e.g. (Proga & Kallman 2004). AGN outflows may be massive enough to have significant implications for our understanding of accretion by supermassive black holes and likely have implications for the interpretation of a wide range of both absorption and emission features in the high energy spectra of AGN (Turner & Miller 2009). However, to properly interpret the observed spectroscopic features, modelling based on realistic theoretical spectra for outflow models is required in order to quantify the flow properties. Here, we have made a significant step towards this goal by extended the code described in Paper I to incorporate the physics of L- and M-shell ions and to compute both the ionization and thermal state of the outflow in detail. This allows us to explore a wider range of plausible outflow conditions including, in particular, less highly-ionized and more optically thick flows.

An example calculation for one of our simply-parameterized wind models illustrates that, for mass-loss rates comparable to the Eddington accretion rate, a wide range of physical conditions are likely to be present in a fast outflow such that a very diverse range of spectral signatures are possible. As in Paper I, we find that considerable complexity can be introduced to the Fe Kα region where both narrow absorption and broad, red-skewed emission lines are predicted to form. However, such an outflow can also significantly affect the spectrum at softer energies – narrow, highly blueshifted absorption lines of lighter elements and lower ionization states of Fe are to be expected for many line-of-sight through an outflow. Emission features associated with these lines also form which can be broadened and skewed in a manner similar to the Fe Kα line, potentially allowing the wind model to account for broad Fe L features as have been reported in the spectrum of 1H0707-495 (see e.g. Fabian et al. 2009; Zoghbi et al. 2009). These features in the soft band are generally weaker that those in the Fe Kα region and their interpretation is more likely to be complicated owing to the wide range of physical components that may affect the softer bands (e.g. the soft excess and/or warm absorbers).

As proof-of-concept, we have presented a simple comparison of our outflow model spectra with the well-known quasar PG1211+143. We found that the most important features that have been identified in its hard X-ray spectra, namely a strong absorption line at ~ 7 keV and a broad emission feature peaking around 6 keV, can be simultaneously well-matched by our theoretical spectra. Although we have not fully explored the possible parameter-space of outflow models nor the interplay with other physically motivated phenomena (such as disk reflection), our results support the interpretation of Pounds & Reeves (2009) that the absorption and emission components are likely physically related and form in a fast outflow that has a substantial covering fraction and a mass-loss rate comparable to the Eddington accretion rate.

Our next step will be to attempt detailed model fits to one or more AGN using our radiative transfer code. This will allow us to more fully test the outflow paradigm and quantify the range of outflow properties which are suggested by observations, a critical step in establishing the role of highly-ionized outflows in the AGN phenomenon.

REFERENCES

Arnaud K. A., 1996, in Jacoby G. H., Barnes J., eds, Astronomical Data Analysis Software and Systems V Vol. 101 of Astronomical Society of the Pacific Conference Series, XSPEC: The First Ten Years. pp 17–+

Arnaud M., Raymond J., 1992, ApJ, 398, 394

Arnaud M., Rothenflug R., 1985, A&AS, 60, 425

Asplund M., Grevesse N., Sauval A. J., 2005, in Barnes III T. G., Bash F. N., eds, Cosmic Abundances as Records of Stellar Evolution and Nucleosynthesis Vol. 336 of Astronomical Society of the Pacific Conference Series, The Solar Chemical Composition. pp 25–+

Auer L. H., van Blerkom D., 1972, ApJ, 178, 175

Cattaneo A., Faber S. M., Binney J., Dekel A., Kormendy J., Mushotzky R., Babul A., Best P. N., Brüggen M., Fabian A. C., Frenk C. S., Khalatyan A., Netzer H., Mahdavi A., Silk J., Steinmetz M., Wisotzki L., 2009, Nature, 460, 213

Dere K. P., Landi E., Mason H. E., Monsignori Fossi B. C., Young P. R., 1997, A&AS, 125, 149

Fabian A. C., Nandra K., Reynolds C. S., Brandt W. N., Otani C., Tanaka Y., Inoue H., Iwasawa K., 1995, MNRAS, 277, L11

Fabian A. C., Zoghbi A., Ross R. R., Uttley P., Gallo L. C., Brandt W. N., Blustin A. J., Boller T., Caballero-Garcia M. D., Larsson J., Miller J. M., Miniutti G., Ponti G., Reis R. C., Reynolds C. S., Tanaka Y., Young A. J., 2009, Nature, 459, 540

Ferland G. J., Korista K. T., Verner D. A., Ferguson J. W., Kingdon J. B., Verner E. M., 1998, PASP, 110, 761

Frank J., King A., Raine D. J., 2002, Accretion Power in Astrophysics: Third Edition

Gu M. F., 2003a, ApJ, 590, 1131

Gu M. F., 2003b, ApJ, 589, 1085

Kaastra J. S., Mewe R., 1993, A&AS, 97, 443

Kallman T., Bautista M., 2001, ApJS, 133, 221

Kallman T. R., Palmeri P., Bautista M. A., Mendoza C., Krolik J. H., 2004, ApJS, 155, 675

---

[4] Although our wind has a total covering fraction of $b = 0.7$, this value cannot be directly compared to that obtained from the much simpler model of Pounds & Reeves (2009) – there is significant diversity in the line-of-sight properties of our model and some of the lines-of-sight through the wind have only very low optical depth.

Kaspi S., Smith P. S., Netzer H., Maoz D., Jannuzi B. T., Giveon U., 2000, ApJ, 533, 631

King A., 2003, ApJL, 596, L27

King A., 2005, ApJL, 635, L121

King A. R., Pounds K. A., 2003, MNRAS, 345, 657

Laming J. M., Titarchuk L., 2004, ApJL, 615, L121

Landi E., Del Zanna G., Young P. R., Dere K. P., Mason H. E., Landini M., 2006, ApJS, 162, 261

Laurent P., Titarchuk L., 2007, ApJ, 656, 1056

Long K. S., Knigge C., 2002, ApJ, 579, 725

Lucy L. B., 1999, A&A, 345, 211

Lucy L. B., 2002, A&A, 384, 725

Lucy L. B., 2003, A&A, 403, 261

Lucy L. B., 2005, A&A, 429, 19

Marziani P., Sulentic J. W., Dultzin-Hacyan D., Calvani M., Moles M., 1996, ApJS, 104, 37

Mendoza C., Kallman T. R., Bautista M. A., Palmeri P., 2004, A&A, 414, 377

Miller L., Turner T. J., Reeves J. N., 2009, MNRAS, 399, L69

Palmeri P., Mendoza C., Kallman T. R., Bautista M. A., 2002, ApJL, 577, L119

Palmeri P., Mendoza C., Kallman T. R., Bautista M. A., 2003, A&A, 403, 1175

Palmeri P., Quinet P., Mendoza C., Bautista M. A., García J., Kallman T. R., 2008, ApJS, 177, 408

Palmeri P., Quinet P., Mendoza C., Bautista M. A., García J., Witthoeft M. C., Kallman T. R., 2008, ApJS, 179, 542

Pounds K. A., Page K. L., 2006, MNRAS, 372, 1275

Pounds K. A., Reeves J. N., 2007, MNRAS, 374, 823

Pounds K. A., Reeves J. N., 2009, MNRAS, 397, 249

Pounds K. A., Reeves J. N., King A. R., Page K. L., O'Brien P. T., Turner M. J. L., 2003, MNRAS, 345, 705

Pounds K. A., Reeves J. N., King A. R., Page K. L., O'Brien P. T., Turner M. J. L., 2005, MNRAS, 356, 1599

Proga D., Kallman T. R., 2004, ApJ, 616, 688

Ross R. R., Fabian A. C., 2005, MNRAS, 358, 211

Schurch N. J., Done C., Proga D., 2009, ApJ, 694, 1

Shull J. M., van Steenberg M., 1982a, ApJS, 49, 351

Shull J. M., van Steenberg M., 1982b, ApJS, 48, 95

Sim S. A., 2005, MNRAS, 356, 531

Sim S. A., Long K. S., Miller L., Turner T. J., 2008, MNRAS, 388, 611

Turner T. J., Miller L., 2009, A&AR, 17, 47

Verner D. A., Ferland G. J., 1996, ApJS, 103, 467

Verner D. A., Ferland G. J., Korista K. T., Yakovlev D. G., 1996, ApJ, 465, 487

Verner D. A., Yakovlev D. G., 1995, A&AS, 109, 125

Zoghbi A., Fabian A. C., Uttley P., Miniutti G., Gallo L. C., Reynolds C. S., Miller J. M., Ponti G., 2009, MNRAS, pp 1772–+